

Sonicated Zeolitic Imidazolate Framework-8 derived Nitrogen-doped hierarchical nanoporous carbon for efficient capture and reversible storage of radioiodine

Elvis Miensah (✉ edmiensah@njust.edu.cn)

Nanjing University of science and technology <https://orcid.org/0000-0002-6167-8021>

Jiuyu Chen

Nanjing University of Science and Technology

Aotian Gu

Nanjing University of Science and Technology

Peng Wang

Nanjing University of Science and Technology

Ying Liu

Nanjing University of Science and Technology

Chunhui Gong

Nanjing University of Science and Technology

Ping Mao

Huaiyin Institute of Technology

Kai Chen

Nanjing University of Information Science and Technology

Yan Jiao

Nanjing University of Information Science and Technology

Zongxiang Zhang

Taizhou environmental monitoring center

Yi Yang

Nanjing University of Science and Technology

Research Article

Keywords: Radioiodine, Zeolitic imidazolate framework-8, adsorption, sonication, porous carbon, metal organic framework

Posted Date: February 18th, 2021

DOI: <https://doi.org/10.21203/rs.3.rs-157131/v1>

License:  This work is licensed under a Creative Commons Attribution 4.0 International License.

[Read Full License](#)

1 **Sonicated Zeolitic Imidazolate Framework-8 derived Nitrogen-doped**
2 **hierarchical nanoporous carbon for efficient capture and reversible storage of**
3 **radioiodine**

4 **Elvis Djam Miensah^a, Jiuyu Chen^a, Aotian Gu^a, Peng Wang^a, Ying Liu^a, Chunhui Gong^a,**
5 **Ping Mao^b, Kai Chen^c, Yan Jiao^c, Zongxiang Zhang^d, Yi Yang^{a, c, *}**

6 ^a Jiangsu Key Laboratory of Chemical Pollution Control and Resources Reuse, School of
7 Environmental and Biological Engineering, Nanjing University of Science and Technology,
8 Nanjing, 210094, China.

9 ^b National & Local Joint Engineering Research Center for Mineral Salt Deep Utilization, Key
10 Laboratory for Palygorskite Science and Applied Technology of Jiangsu Province, School of
11 Chemical Engineering, Huaiyin Institute of Technology, Huaian 223003, China

12 ^c Collaborative Innovation Center of Atmospheric Environment and Equipment Technology,
13 Jiangsu Key Laboratory of Atmospheric Environment Monitoring and Pollution Control
14 (AEMPC), Nanjing University of Information Science & Technology, Nanjing 210044, China.

15 ^d Jiangsu Environmental Protection Key Laboratory of Monitoring for Organic Pollutants in Soil,
16 Taizhou Environmental Monitoring Center, Taizhou, 225300, China.

17 * Corresponding author: yangyi@njust.edu.cn; Jiangsu Key Laboratory of Chemical Pollution
18 Control and Resources Reuse, School of Environmental and Biological Engineering, Nanjing
19 University of Science and Technology, Nanjing 210094, China. Tel/Fax: +86-25-8431-1956

20

21 **Abstract**

22 Iodine plays a significant role in industry and in chemical processes within living organisms.
23 However, radioiodine exposure possess threats such as thyroid cancer to humans, when they are
24 released into the environment when using nuclear technology and through nuclear accidents. Its
25 capture and storage is critical to safeguard industrial applications while preventing
26 environmental leakages. Herein we report efficient radioiodine capture using a hierarchical
27 nitrogen-doped, large surface area, nanoporous carbon derived from ultrasonication of ZIF-8.

28 The carbon exhibited high adsorption capacity of 434 wt% gravimetrically and 1418 mgg⁻¹ in
29 cyclohexane solution with fast kinetics and high recoverability. We deduced the high adsorption
30 capacity to be due to the large surface area with micro and mesopores, presence of hydroxyl
31 groups acting as electron donors and the presence of nitrogen, which interacts strongly with the
32 electron-deficient iodine (I₂). Moreover, the process best fits the pseudo-second-order and
33 Freundlich models with multilinearity observed with Webber-Morris model. Because of its
34 comparatively lower cost, large surface area, facile preparation, good regeneration and fast
35 kinetics, the as-prepared porous carbon shows exceptional promise as radioiodine adsorbent.

36 **Keywords: Radioiodine, Zeolitic imidazolate framework-8, adsorption, sonication, porous**
37 **carbon, metal organic framework**

38 **1.0 Introduction**

39 Increasing world energy demands because of rising population, coupled with industrialization
40 and reduction in traditional fossil fuels has made the need for alternative energy sources more
41 important. Nuclear energy has come as a source of choice as it does not emit greenhouse gases.
42 Countries such as the United States of America, France, United Kingdom and China have
43 adopted this option to mitigate this problem (Patzek and Croft 2010), (Kaltsoyannis and Liddle
44 2016). However, it is worrying to note that with this proliferation of nuclear technology comes
45 the emission of radionuclides. Key among these is radioactive iodine, which is a fission product
46 of fissile Uranium-235. The accidents in Chernobyl, 3 mile island and recently Fukushima for
47 instance have released large amounts of radioiodine into the environment (Wang et al. 2018),
48 (Hobbs et al. 2011). Due to its high volatility, long half-life (1.57×10^7 for the ¹²⁹I isotope), easy
49 dissolution in water and adverse effects on human metabolic processes, radioiodine has drawn
50 significant attention from the scientific world recently. Though the ¹³¹I isotope has a half-life of
51 8.02 days, its thyroid cancer causing potential in children makes its removal from the
52 environment very important (Prisyazhiuk et al. 1991), (Cardis et al. 2005). The adsorption
53 technology has seen commonplace in iodine removal due to its easy operation, large-scale
54 deployment potential and very economical. However, it requires a very efficient adsorbent in
55 order to be successfully deployed. Many adsorbent materials have been used for iodine
56 sequestration over the years including silver-containing mordenites, (Chapman et al. 2010),
57 Metal organic and covalent organic frameworks (Sava et al. 2011), (Nandanwar et al. 2016), (Yu

58 et al. 2015), (Sun et al. 2013); and aerogels (Riley et al. 2013), (Riley et al. 2014), (Adams and
59 Weller 2018), (Huang et al. 2017), (Kobielska et al. 2018), (Shen et al. 2018). Amine-
60 impregnated activated carbon, silica and zeolites are also used extensively (Liu et al. 2015),
61 (Subrahmanyam et al. 2015). The challenges with these adsorbents however limit their efficiency.
62 For instance, organic amine ages easily and makes the potential for secondary pollution very
63 high as captured iodine could leak into the environment. Moreover, small pore sizes of activated
64 carbon makes for low adsorption capacity. In addition, low recovery and recyclability
65 percentages makes the need for more efficient adsorbents even more important.

66 Recently, porous carbons have drawn attention in gas storage and separation applications, water
67 purification and catalysis due to their highly developed porosities, large specific surface areas,
68 good recycling ratios and robust thermal and chemical stability (Han et al. 2020).(Sun et al.
69 2017). Additionally, they have been highlighted as promising adsorbents in many reports
70 because of their environmental friendliness and tunable textural and structural properties (Yang
71 et al. 2012), (Sevilla et al. 2011), (Nandi et al. 2012), (Qian et al. 2014). The challenge is to
72 obtain efficient adsorbent with favorable properties for efficient radioiodine removal while
73 reducing cost. Zeolitic Imidazolate Frameworks (ZIFs) belong to the Metal Organic Framework
74 family but combine the classical zeolite properties of chemical and thermal stability with the rich
75 topological diversity of MOFs. ZIFs possess similar structures to aluminosilicate zeolites, but
76 with the additional advantageous characteristics MOFs (Miensah et al. 2019). These make them
77 suitable precursors for porous carbons as the favorable characteristics of the ZIFs are retained in
78 the corresponding porous carbons. Recently Amali and co-workers developed porous carbon
79 materials where meso, macropores were introduced into the synthesized materials to obtain
80 hierarchical, highly porous carbons with efficient supercapacitor properties (Amali et al. 2014).
81 Based on these we prepared a nitrogen doped nanoporous hierarchical carbon by ultrasonication
82 of ZIF-8 precursor. Ultrasonication introduced mesopores as additional second order structures,
83 which enhanced radioiodine adsorption. No report highlights radioiodine adsorption with
84 nanoporous carbon derived by ultrasonication of the ZIF-8 precursor, to the best of our
85 knowledge. The as-synthesized nanoporous carbon displayed very high radioiodine adsorption
86 and exhibited exceptional recyclability, boosting its practical application potential.

87 **2.0 Materials and method**

88 **2.1 Chemicals**

89 Zinc nitrate hexahydrate ($\text{Zn}(\text{NO}_3)_2 \cdot 6\text{H}_2\text{O}$, $\geq 99.9\%$), 2-methylimidazole (MeIm, $\geq 99.0\%$,
90 Aldrich), triethylamine (TEA, $\geq 99.0\%$, Aldrich),

91 **2.2 Instrumentation**

92 We used the bath sonicator model VELVO, VS-N100S, at 100 W, and 40 kHz for the
93 ultrasonication stage. Scanning electron microscope (SEM) model FEI Quanta FEG, USA,
94 Powder X-ray diffraction (PXRD) with Bruker D8 Advance X-ray diffractometer, equipped with
95 $\text{Cu K}\alpha$ radiation at 40 kV and 40 mA. X-ray photoelectron spectroscopy (XPS) model PHI
96 Quantera II electron spectrometer, equipped with a monochromatic $\text{Al K}\alpha$ radiation.
97 Transmission electron microscope (TEM), model Tecnai G2 F30 S-Twin TEM with voltage
98 200 kV. Brunauer–Emmett–Teller (BET) method (ASAP-2020, USA) at 77 K.

99 **2.3 Preparation of materials**

100 **2.3.1 Preparation of sonicated ZIF-8**

101 Synthesis was according to the literature with modifications (Amali et al. 2014). Briefly methanol
102 solution (250 ml) with 3.7273 g of $\text{Zn}(\text{NO}_3)_2 \cdot 6\text{H}_2\text{O}$ was added into a 250 ml methanol of 1.1747
103 g 2-methylimidazole (MeIm) and 2.25 ml of triethylamine (TEA) under ultrasonication for 10
104 minutes at ambient temperature for a turbid solution immediately. Nucleation and aging was
105 allowed for 4 hours before centrifugation to obtain white solid which was washed 3 times with
106 methanol before drying at 65°C for 24 hours to obtain sonicated ZIF-8 captioned s-ZIF-8

107 **2.3.2 Synthesis of sonicated ZIF-8 nanoporous carbon**

108 1.5g of s-ZIF-8 was transferred into a ceramic boat, calcined at 800°C for 4 hours in nitrogen
109 atmosphere using a programmable furnace with $10^\circ\text{C min}^{-1}$ heating rate. The resultant carbon
110 material was then activated using potassium hydroxide (KOH). Briefly, KOH was ground with
111 the as-synthesized carbon in a 3:1 ratio, transferred into a ceramic boat and calcined in a
112 programmable furnace under nitrogen flow for 1 hour at a $10^\circ\text{C min}^{-1}$ heating rate. The porous
113 carbon obtained was then washed with 1M HCl; and then deionized water to remove residual
114 zinc. The final sonicated nitrogen-doped hierarchical carbon obtained was captioned s-ZNPC.
115 For comparison ZIF-8 as was prepared without sonication and was directly carbonized and
116 activated with KOH to obtain ZNPC.

117 **2.4 Adsorption and storage of Iodine**

118 Iodine uptake was studied by exposing the as-prepared carbon materials to iodine
119 (nonradioactive) in a vessel tightly sealed at 353 K and atmospheric pressure for specific times.
120 The vessel was then cooled and we took weight measurements and calculated iodine uptake as

$$121 \quad (m_2 - m_1) / m_1 \times 100\text{wt}\% \quad (1)$$

122 Where m_1 is the adsorbent mass before adsorption and m_2 is the adsorbent mass after adsorption.
123 We studied iodine adsorption in cyclohexane by placing 10mg of the as-prepared adsorbent in 10
124 ml iodine in cyclohexane solution for a while. Approximately 2 mL supernatant was then taken
125 and evaluated with UV–Vis. iodine (I_2) amount at equilibrium q_e was then obtained using Eqn.2:

$$126 \quad q_e = v \frac{(c_0 - c_e)}{m} \quad (2)$$

127 With v signifying iodine/cyclohexane solution volume in liters, C_o denotes initial concentration
128 of iodine/cyclohexane solution and C_e denotes equilibrium concentration of iodine/cyclohexane
129 solution in mgL^{-1} ; and m is the mass of the adsorbent in grams. We evaluated removal efficiency
130 with Eqn. 3:

$$131 \quad \text{Removal efficiency} = \left(\frac{C_o - C_e}{C_o} \right) \times 100\% \quad (3)$$

132 C_o signifies initial concentration and C_e denotes equilibrium concentration of iodine/cyclohexane
133 solution. We performed all the experiments in triplicates to obtain reproducible results and
134 calculated errors using a 95% confidence level of the standard deviation from the origin-9 pro
135 software. We used weber-Morris model, pseudo-first-order model and pseudo-second-order
136 model (Hosseini et al. 2011) to study the adsorption kinetics. The pseudo-first-order kinetic
137 model is depicted by eqn.4 below:

$$138 \quad \ln(q_e - q_t) = k_1 t + \ln q_e \quad (4)$$

139 With q_e representing equilibrium adsorption capacity and q_t representing adsorption capacity at
140 time t , and k_1 is adsorption rate constant. Rate constant value and adsorption capacity values
141 were obtained using the intercept value and slope value after plotting $\ln(q_e - q_t)$ vs. t .

142 Eqn. 5 below displays the pseudo-second-order kinetic model:

143
$$\frac{t}{q_t} = \frac{1}{k_2 q_e^2} + \frac{t}{q_e} \quad (5)$$

144 With k_2 representing rate constant, q_e representing equilibrium adsorption capacity while q_t
145 represents adsorption capacity at a certain time (t). k_2 (intercept) and q_e (slope) were derived
146 from plotting t/q_t vs. t .

147 The Weber-Morris model is depicted by eqn.6 below:

148

149
$$q_t = k_d t^{0.5} + c \quad (6)$$

150 Where, k_d represents the diffusion rate constant with c denoting the intercept, which were derived
151 by plotting q_t against $t^{0.5}$.

152 Adsorption isotherm studies were also performed using the Freundlich and Langmuir models
153 represented by equations 7 and 8 below respectively

154
$$\ln q_e = \ln k_F + \frac{1}{n} \ln c_e \quad (7)$$

155 With K_F (mgg^{-1}), being the Freundlich constant, associated with adsorption capacity and n being
156 Freundlich constant associated with adsorption intensity, which we derived from the slope (K_F)
157 and intercept (n) value after plotting $\ln q_e$ vs $\ln C_e$

158
$$\frac{c_e}{q_e} = \frac{1}{k_L q_m} + \frac{1}{q_m} c_e \quad (8)$$

159 Where C_e (mgL^{-1}) is equilibrium iodine concentration, q_e (mgg^{-1}) is equilibrium adsorbed amount,
160 q_m (mgg^{-1}) represents maximum amount of iodine adsorbed, and K_L (Lmg^{-1}) represents
161 equilibrium adsorption constant. By plotting C_e/q_e vs. C_e , we obtained q_m and K_L from the slope
162 and intercept respectively.

163

164 **2.5 Characterization**

165 PXRD (Powder X-ray diffraction) was performed with a Bruker D8 Advance X-ray
166 diffractometer with Cu K α radiation at 40 kV and 40 mA. Raman spectra was recorded with a
167 LabRAM HR800 Raman spectrometer with sample excitation at 532 nm. XPS was recorded with
168 PHI Quantera II electron spectrometer. N₂ adsorption-desorption analysis was done using
169 Quantachrome Autosorb-iQ MP gas sorptometer at 77k, while BET method was adopted to
170 evaluate the specific surface areas using N₂ adsorption data. Pore size distribution was evaluated
171 using the NLDFT (Non-localized Density Functional Theory) method. SEM (Scanning Electron
172 Microscope) image as taken with JEOS JSM-IT500HR system while TEM scan was done on a
173 FEI (Tecnai G2 TF20) microscope. The concentration of I₂ in the supernatants were measured
174 with UV–vis spectrophotometer.

175

176

177

178

179

180

181

182

183

184

185

186

187

188

189

190

191

192

193 **3.0 Results and discussion**

194 **3.1 Structural analysis**

195 We prepared the porous carbon samples s-ZNPC and ZNPC by ultrasonication and carbonization
196 of ZIF-8 precursor as outlined in the experimental section and further deployed chemical
197 activation by KOH to introduce pores by etching the carbon framework. KOH activation resulted
198 in increased surface area and introduced hydroxyl groups on the porous carbon material. As can
199 be observed from the PXRD (fig.2a), both carbon sample exhibit peaks at $2\theta = 25^\circ$ and 42°
200 which correspond to the 002 and 100 planes of amorphous carbon materials respectively
201 indicating the successful formation of the carbon samples(Hu et al. 2020). The broad 002 Bragg
202 peak is an indication of low graphitization. The empirical parameter (R), which measures the
203 ratio of peak to background, showed a lower value for s-ZNPC than ZNPC. This shows aligned
204 structural domain breakdown in s-ZNPC after KOH activation as reported in the literature (Sun
205 et al. 2017). Moreover, the poorly crystallized nature as well as low graphitization could be
206 observed. During KOH activation of s-ZNPC the carbon framework is etched due to carbon atom
207 being oxidized to carbonate ion. In addition to this, there is also potassium compounds
208 intercalation (K_2CO_3), decomposition of which results in the emission of CO_2 through carbon
209 gasification, leading to formation of more pores in the carbon material. PXRD also confirms that
210 KOH activation resulted in decreased low-angle peak intensity of s-ZNPC consistent with the
211 literature (Choi and Ryoo 2007). This is also an indication of the significant structural change to
212 the carbon framework by KOH activation.

213

214 The Raman spectra was taken to analyze the degree of order in the porous carbon samples
215 (fig.2b). The 1592cm^{-1} peak position also known as G-band is consistent in all sp^2 carbon
216 systems as well as the E_{2g} graphite mode. The second peak located at 1348cm^{-1} also known as
217 the D-band indicates disorder in carbon materials (Sun et al. 2017). The relative disorder in
218 graphitic crystallinity is normally determined by the integrated intensity ratio of the D-band to
219 the –band, denoted I_D/I_G . the higher intensity ratio for s-ZNPC (1.01) as opposed to ZNPC (0.976)
220 indicates higher defects after KOH activation which enhanced its adsorption properties (Qie et al.
221 2013), (Sun et al. 2017). The XPS of the samples before and after iodine adsorption is shown in
222 fig. 4. The survey spectra (fig. 4a) shows a high carbon and oxygen content, confirming further
223 the high degree of oxidation of the as-prepared sample. Moreover, nitrogen is confirmed
224 successfully doped into the material and the appearance of the iodine peak after adsorption
225 confirms that the porous carbon samples captured iodine successfully. The high resolution C1s
226 spectra (fig.4c) of s-ZNPC exhibits three peaks at binding energies 286.6eV, 285.1eV and
227 284.4eV corresponding to O-C=C, C-N and C-C carbon species respectively (Hu et al. 2020).
228 The deconvoluted N1s spectra (fig.4b) also shows four peaks at 406.3eV, 401.2eV, 400.0eV and
229 397.0eV representing oxidized, graphitic, pyrrolic and pyridinic nitrogen species respectively
230 (Xiao et al. 2018). The deconvoluted I3d spectra (fig.4d) also displays two distinct peaks at
231 binding energies 620.0eV and 630.2eV which resulted from spin orbit splitting of $I3d_{5/2}$ and
232 $I3d_{3/2}$ respectively with splitting energy of 10.2eV. These are consistent with molecular iodine
233 and iodide (Kajan et al. 2016), (Dillard et al. 1984), (Sherwood 1976). The presence of iodide
234 could have resulted from reduction of molecular iodine (I_2) by hydroxyl groups (OH^-) present on
235 the carbon surface acting as electron pair donors (Flockhart 1974), (Gliński and Ulkowska 2011).

236

237

238

239

240

241

242

243

244
245
246
247
248
249
250
251
252
253
254
255
256
257
258
259
260
261
262
263
264
265
266
267
268
269
270
271
272
273

3.2 Morphological studies

Careful observation of the SEM and TEM (fig.1) images show a highly porous structure for both carbon samples with s-ZNPC (fig.1a) showing a uniform distribution of micro and mesopores. TEM image of s-ZNPC (fig. 1b) confirms the presence of aperiodic and hierarchical pore structure with micro and mesoporous three-dimensional structure. It could also be seen that s-ZNPC is poorly crystallized with little parallel graphene sheets observed, consistent with the Raman and PXRD results. Quantification of the surface textural features was achieved by measuring the nitrogen (N₂) adsorption-desorption curves and as can be observed in fig.S1, a varied type I and type IV isotherms were obtained. Distinct plateaus could be seen in the isotherms, confirming the hierarchical pore structure of as-prepared carbons with dominant mesoporosity in s-ZNPC (fig.S1a-b) and microporosity being dominant in ZNPC (fig. S1c-d). The N₂ adsorption isotherms at 77k display a strong adsorption at low pressure for both carbon samples, indicating microporosity. However, mesoporosity is also observed by the appearance of hysteresis loop at relative pressure range 0.4 to 0.9. The BET surface areas were calculated to be 2350 m²g⁻¹ for s-ZNPC with pore volume 1.4 cm³g⁻¹ and 1899 m²g⁻¹ for ZNPC with pore volume 1.12 cm³g⁻¹ (tab. S1). We employed the non-local density functional theory method (NL-DFT) to evaluate pore size distribution of the materials. The results further confirm that s-ZNPC has hierarchical pore structure with micropores (< 2nm) and mesopores (2-50 nm); but with a higher mesopore density than ZNPC.

274 **3.3 Radioiodine capture**

275 Encouraged by the large surface area and porous features of as-prepared carbon samples, we
276 investigated their iodine adsorption capacity by exposing them to iodine in a sealed container at
277 350K and atmospheric pressure for various time intervals. These conditions represent nuclear
278 fuel reprocessing conditions (Qian et al. 2016). We substituted radioisotopes ^{131}I and ^{129}I for
279 stable ^{127}I that has similar chemical characteristics to the radioisotopes. We then took gravimetric
280 measurements at various time intervals. It could be observed in fig.2c that adsorption of iodine
281 increased with time up to 5 hours. Changes were not observed after about 11 hours, which
282 signifies the saturation point of the adsorption process. Maximum adsorption capacity of 434
283 wt% was obtained for s-ZNPC and 342 wt% for ZNPC after calculations using eqn.1. We
284 believe this high adsorption capacity could be the result of the large surface area with
285 hierarchical micro and mesopores introduced through ultrasonication and KOH activation. In
286 addition to the above, the high iodine capacity could be attributed to the nitrogen-rich nature of
287 these porous carbons due to the strong interaction between nitrogen atoms and electron-deficient
288 iodine (I_2); consistent with the literature (Sen et al. 2020). Moreover, XPS results (fig.4) also
289 confirm the captured iodine as in the zero valence state (I_2). This capacity is the highest reported
290 for sonicated ZIF-8-derived carbons to the best of our knowledge. It is also higher than most
291 porous sorbents reported to date (Qian et al. 2016), (Sun et al. 2017),(Liu et al. 2011), (A et al.
292 2014), (Sava et al. 2013), (Chien et al. 2011),(Zhou et al. 2014), (Riley et al. 2011), (Liu et al.
293 2011), (Yin et al. 2012), (Sava et al. 2011), (Huang et al. 2012), (A et al. 2014).

294

295 We also investigated iodine capture by as-prepared carbon materials in iodine/cyclohexane
296 solution, and observed an initial increase in adsorption amount, which then decreased slowly as
297 equilibrium is reached after 30 hours (fig. We calculated the maximum adsorbed amount for s-
298 ZNPC using eqn. 2 to be 87 mgg^{-1} , 238 mgg^{-1} and 305 mgg^{-1} for iodine/cyclohexane solution
299 concentrations 100 mg/L, 300 mg/L and 500 mg/L respectively. Removal efficiencies of 87%,
300 70% and 61% were observed for solution concentrations 100, 300 and 500 mg/L respectively
301 (fig.3). The concentration of the solution and contact time affected the adsorption process.
302 Clearly, the adsorbed amount increased in high concentrations while the efficiency of the
303 adsorption decreased. The equilibrium adsorption isotherm displayed in figure 2d is very
304 important in deducing the maximum adsorption capacity of the porous carbons. The amount was
305 found to be 1418 mgg^{-1} for s-ZNPC, which is the highest ever reported for sonicated ZIF-8-
306 derived porous carbon for I_2 adsorption, to the best of our knowledge. We deduced this high
307 value to be due to the large surface area, high porosity (micro, mesopores) and the presence of
308 hydroxyl groups (OH^-) serving as electron pair donors on the porous carbon surface. Moreover,
309 the presence of heteroatom nitrogen enhanced the adsorption capacity for radioiodine, due to the
310 strong interaction between nitrogen atoms and electron-deficient iodine (I_2); consistent with the
311 literature (Song et al. 2018), (Sen et al. 2020).

312
313 The plot of equilibrium concentration (C_e) versus the equilibrium amount (q_e) (fig. 2d) showed
314 that the initial adsorption depended on the initial concentration of the solution, where there was
315 high amounts of iodine in solution ('host-guest interaction'). However, this changed as the
316 adsorption reached equilibrium as iodine amounts dropped in the solution ('guest-guest effect'),
317 consistent with the literature (Li et al. 2020), (Geng et al. 2018). We simulated the adsorption
318 isotherm using the Freundlich (eqn. 7, fig.S2b) and Langmuir models (eqn. 8, fig.S2a). From the
319 fitting parameters in table S2, Freundlich model best fits the adsorption process due to its higher
320 correlation (0.998). In addition to the above, its adsorption intensity ($n=4.45$) indicates a
321 favorable adsorption ($1 < n < 10$). We inferred from these data that the adsorption is a multilayer
322 process on a multiphase surface as reported in the literature (Geng et al. 2018).

323 We also investigated adsorption kinetics using the pseudo-first-order model (eqn.4, fig. S2c),
324 pseudo-second-order model (eqn.5, fig.S2d) and weber-Morris model (eqn.6) and found the
325 pseudo-second-order model as the best fit for the adsorption process, indicating a chemisorption
326 process (table S3). This is because it has a higher correlation with the calculated adsorption
327 capacity closer to the experimental values as previously reported (Geng et al. 2018). Moreover,
328 we adopted the Webber-Morris model to evaluate the adsorption mechanism and found the
329 adsorption process to be multi-linear as seen in fig. S4. This implies that the adsorption process
330 involved more than one stage. From fig. S4, the initial stage is indicative of iodine molecules
331 diffusing onto the outer surface of s-ZNPC while the second stage could be attributed to
332 intraparticle diffusion leading to saturation or equilibrium as reported in previous literature
333 (Hosseini et al. 2011). The captured iodine was quickly recovered by immersing the I₂-loaded
334 sample captioned I₂@s-ZNPC into ethanol solution and taking UV-Vis measurements until there
335 was no further change in concentration of the iodine solution (fig. S.3).

336
337
338
339
340
341
342
343
344
345
346
347
348
349
350
351

352 **4.0 Conclusion**

353 Briefly, we synthesized nitrogen-doped, hierarchical porous carbon by ultrasonication of ZIF-8
354 to introduce additional mesopores as secondary structures, activated the porous carbon using
355 KOH to introduce hydroxyl groups and increase the surface area. We took advantage of the
356 favorable features of the as-prepared carbon (s-ZNPC) for capture and reversible release of
357 radioiodine. We obtained very high adsorption capacity of 434 wt% after gravimetric
358 measurements and 1418 mgg⁻¹ in cyclohexane solution. These values rank among the highest for
359 nanoporous carbons obtained by sonication of ZIF-8 precursor. We also found the adsorption
360 data to fit with the pseudo-second-order and Freundlich models. We achieved desorption easily
361 by immersing the iodine-loaded sample (I₂@s-ZNPC) into ethanol solution and took UV-Vis
362 measurements. The high adsorption capacity, relatively faster kinetics, easy preparation and
363 recoverability make s-ZNPC a promising candidate for radioiodine adsorption and could be very
364 essential in decontaminating the environment of radioactive iodine.

365

366 **Declarations**

367 **Acknowledgments**

368 The work was partially funded by the National Natural Science Foundation of China (No.
369 51908240 and 11205089), the Natural Science Foundation of Jiangsu Province (No.
370 BK20181064), and Jiangsu Engineering Technology Research Center of Environmental
371 Cleaning Materials (No. KFK1504).

372 **Author contributions**

- 373 1- Kai Chen: Supervision, Writing - Review & Editing
- 374 2- Chunhui Gong: Supervision, Writing - Review & Editing
- 375 3- Jiu Yu Chen: Software, Investigation
- 376 4- Peng Wang: Supervision, Writing - Review & Editing
- 377 5- Zong Xian Zhang: Investigation, Writing - Review & Editing

- 378 6- Yan Jiao : Validation, Investigation
- 379 7- Ying Liu: Validation, Writing - Review & Editing
- 380 8- Ping Mao: Writing - Review & Editing
- 381 9- Aotian Gu: Writing - Review & Editing
- 382 10-Elvis Djam Miensah : Writing - Original Draft, Methodology, Conceptualization,
383 Investigation
- 384 11- Yi Yang - Funding acquisition, Project administration, Supervision, Resources

385 **Conflicts of interest or competing interests**

386 The named authors do not have any commercial or associative interest that represents a
387 conflict of interest in connection with the work submitted.

388 **Data and code availability**

389 Not applicable

390 **Supplementary information**

391 Supplementary file contains some figures and tables to buttress some points made in the main
392 text

393 **Ethical approval**

394 Not applicable

395 **Consent to participate**

396 Not applicable

397 **Consent to publish**

398 Not applicable

399

400

401
402
403
404
405
406
407
408
409
410
411
412
413
414
415
416
417
418
419
420
421
422
423
424
425
426
427
428
429
430
431
432
433
434
435
436

References

- A S, Zhang Y, Li Z, et al (2014) Highly efficient and reversible iodine capture using a metalloporphyrin-based conjugated microporous polymer. *Chem Commun* 50:8495–8498. <https://doi.org/10.1039/C4CC01783H>
- Adams GM, Weller AS (2018) POP-type ligands: Variable coordination and hemilabile behaviour. *Coord Chem Rev* 355:150–172. <https://doi.org/10.1016/j.ccr.2017.08.004>
- Amali AJ, Sun JK, Xu Q (2014) From assembled metal-organic framework nanoparticles to hierarchically porous carbon for electrochemical energy storage. *Chem Commun* 50:1519–1522. <https://doi.org/10.1039/c3cc48112c>
- Cardis E, Kesminiene A, Ivanov V, et al (2005) Risk of thyroid cancer after exposure to ¹³¹I in childhood. *J Natl Cancer Inst* 97:724–732. <https://doi.org/10.1093/jnci/dji129>
- Chapman KW, Chupas PJ, Nenoff TM (2010) Radioactive iodine capture in silver-containing mordenites through nanoscale silver iodide formation. *J Am Chem Soc* 132:8897–8899. <https://doi.org/10.1021/ja103110y>
- Chien C-C, Huang Y-P, Wang W-C, et al (2011) Efficiency of Moso Bamboo Charcoal and Activated Carbon for Adsorbing Radioactive Iodine. *CLEAN - Soil, Air, Water* 39:103–108. <https://doi.org/10.1002/clen.201000012>
- Choi M, Ryoo R (2007) Mesoporous carbons with KOH activated framework and their hydrogen adsorption. *J Mater Chem* 17:4204. <https://doi.org/10.1039/b704104g>
- Dillard JG, Moers H, Klewe-Nebenius H, et al (1984) An x-ray photoelectron and Auger electron spectroscopic study of the adsorption of molecular iodine on uranium metal and uranium dioxide. *J Phys Chem* 88:4104–4111. <https://doi.org/10.1021/j150662a050>
- Flockhart B (1974) Electron-transfer at alumina surfaces 4. Reduction of iodine. *J Catal* 32:20–24. [https://doi.org/10.1016/0021-9517\(74\)90154-7](https://doi.org/10.1016/0021-9517(74)90154-7)
- Geng T, Chen G, Xia H, et al (2018) Poly{tris[4-(2-thienyl)phenyl]amine} and poly[tris(4-carbazoyl-9-yl phenyl)amine] conjugated microporous polymers as absorbents for highly efficient iodine adsorption. *J Solid State Chem* 265:85–91. <https://doi.org/10.1016/j.jssc.2018.05.030>
- Gliński M, Ulkowska U (2011) Reaction of iodine with metal oxides. *Can J Chem* 89:1370–1374. <https://doi.org/10.1139/v11-117>

437 Han T-T, Wang L-N, Potgieter JH (2020) ZIF-11 derived nanoporous carbons with ultrahigh
438 uptakes for capture and reversible storage of volatile iodine. *J Solid State Chem* 282:121108.
439 <https://doi.org/10.1016/j.jssc.2019.121108>

440 Hobbs DT, Peters TB, Taylor-Pashow KML, Fink SD (2011) Development of an improved
441 titanate-based sorbent for strontium and actinide separations under strongly alkaline
442 conditions. *Sep Sci Technol* 46:119–129. <https://doi.org/10.1080/01496395.2010.492772>

443 Hosseini S, Khan MA, Malekbala MR, et al (2011) Carbon coated monolith, a mesoporous
444 material for the removal of methyl orange from aqueous phase: Adsorption and desorption
445 studies. *Chem Eng J* 171:1124–1131. <https://doi.org/10.1016/j.cej.2011.05.010>

446 Hu L, Xu Z, He P, et al (2020) Zinc and Nitrogen-Doped Carbon In-Situ Wrapped ZnO
447 Nanoparticles as a High-Activity Catalyst for Acetylene Acetoxylation. *Catal Letters*
448 150:1155–1162. <https://doi.org/10.1007/s10562-019-02971-9>

449 Huang N, Zhai L, Xu H, Jiang D (2017) Stable Covalent Organic Frameworks for Exceptional
450 Mercury Removal from Aqueous Solutions. *J Am Chem Soc* 139:2428–2434.
451 <https://doi.org/10.1021/jacs.6b12328>

452 Huang PS, Kuo CH, Hsieh CC, Horng YC (2012) Selective capture of volatile iodine using
453 amorphous molecular organic solids. *Chem Commun* 48:3227–3229.
454 <https://doi.org/10.1039/c2cc17716a>

455 Kajan I, Tietze S, Ekberg C (2016) Interaction of ruthenium tetroxide with iodine-covered
456 surfaces of materials in nuclear reactor containment building. *J Nucl Sci Technol* 53:1889–
457 1898. <https://doi.org/10.1080/00223131.2016.1174627>

458 Kaltsoyannis N, Liddle ST (2016) Catalyst: Nuclear Power in the 21st Century. *Chem* 1:659–662.
459 <https://doi.org/10.1016/j.chempr.2016.10.003>

460 Kobielska PA, Howarth AJ, Farha OK, Nayak S (2018) Metal–organic frameworks for heavy
461 metal removal from water. *Coord Chem Rev* 358:92–107.
462 <https://doi.org/10.1016/j.ccr.2017.12.010>

463 Li G, Huang Y, Lin J, et al (2020) Effective capture and reversible storage of iodine using foam-
464 like adsorbents consisting of porous boron nitride microfibers. *Chem Eng J* 382:122833.
465 <https://doi.org/10.1016/j.cej.2019.122833>

466 Liu Q-K, Ma J-P, Dong Y-B (2011) Highly efficient iodine species enriching and guest-driven
467 tunable luminescent properties based on a cadmium(ii)-triazole MOF. *Chem Commun*
468 47:7185. <https://doi.org/10.1039/c1cc11402f>

469 Liu S, Wang N, Zhang Y, et al (2015) Efficient removal of radioactive iodide ions from water by
470 three-dimensional Ag₂O–Ag/TiO₂ composites under visible light irradiation. *J Hazard*
471 *Mater* 284:171–181. <https://doi.org/10.1016/j.jhazmat.2014.10.054>

472 Miensah ED, Khan MM, Chen JY, et al (2019) Zeolitic imidazolate frameworks and their
473 derived materials for sequestration of radionuclides in the environment: A review. *Crit Rev*
474 *Environ Sci Technol* 1–61. <https://doi.org/10.1080/10643389.2019.1686946>

475 Nandanwar SU, Coldsnow K, Utgikar V, et al (2016) Capture of harmful radioactive

476 contaminants from off-gas stream using porous solid sorbents for clean environment – A
477 review. *Chem Eng J* 306:369–381. <https://doi.org/10.1016/j.cej.2016.07.073>

478 Nandi M, Okada K, Dutta A, et al (2012) Unprecedented CO₂ uptake over highly porous N-
479 doped activated carbon monoliths prepared by physical activation. *Chem Commun*
480 48:10283. <https://doi.org/10.1039/c2cc35334b>

481 Patzek TW, Croft GD (2010) A global coal production forecast with multi-Hubbert cycle
482 analysis. *Energy* 35:3109–3122. <https://doi.org/10.1016/j.energy.2010.02.009>

483 Prisyazhiuk A, Pjatak OA, Buzanov VA, et al (1991) Cancer in the Ukraine, post-Chernobyl.
484 *Lancet* 338:1334–1335. [https://doi.org/10.1016/0140-6736\(91\)92632-C](https://doi.org/10.1016/0140-6736(91)92632-C)

485 Qian D, Lei C, Wang E-M, et al (2014) A Method for Creating Microporous Carbon Materials
486 with Excellent CO₂ Adsorption Capacity and Selectivity. *ChemSusChem* 7:291–298.
487 <https://doi.org/10.1002/cssc.201300585>

488 Qian X, Zhu ZQ, Sun HX, et al (2016) Capture and Reversible Storage of Volatile Iodine by
489 Novel Conjugated Microporous Polymers Containing Thiophene Units. *ACS Appl Mater*
490 *Interfaces* 8:21063–21069. <https://doi.org/10.1021/acsami.6b06569>

491 Qie L, Chen W, Xu H, et al (2013) Synthesis of functionalized 3D hierarchical porous carbon for
492 high-performance supercapacitors. *Energy Environ Sci* 6:2497–2504.
493 <https://doi.org/10.1039/c3ee41638k>

494 Riley BJ, Chun J, Ryan J V., et al (2011) Chalcogen-based aerogels as a multifunctional platform
495 for remediation of radioactive iodine. *RSC Adv* 1:1704. <https://doi.org/10.1039/c1ra00351h>

496 Riley BJ, Chun J, Um W, et al (2013) Chalcogen-Based Aerogels As Sorbents for Radionuclide
497 Remediation. *Environ Sci Technol* 47:7540–7547. <https://doi.org/10.1021/es400595z>

498 Riley BJ, Pierce DA, Chun J, et al (2014) Polyacrylonitrile-chalcogel hybrid sorbents for
499 radioiodine capture. *Environ Sci Technol* 48:5832–5839.
500 <https://doi.org/10.1021/es405807w>

501 Sava DF, Chapman KW, Rodriguez MA, et al (2013) Competitive I₂ sorption by Cu-BTC from
502 humid gas streams. *Chem Mater* 25:2591–2596. <https://doi.org/10.1021/cm401762g>

503 Sava DF, Rodriguez MA, Chapman KW, et al (2011) Capture of volatile iodine, a gaseous
504 fission product, by zeolitic imidazolate framework-8. *J Am Chem Soc* 133:12398–12401.
505 <https://doi.org/10.1021/ja204757x>

506 Sen S, Al-Sayah MH, Mohammed MS, et al (2020) Multifunctional nitrogen-rich aminal-linked
507 luminescent porous organic polymers for iodine enrichment and selective detection of Fe³⁺
508 ions. *J Mater Sci* 55:10896–10909. <https://doi.org/10.1007/s10853-020-04741-0>

509 Sevilla M, Valle-Vigón P, Fuertes AB (2011) N-Doped Polypyrrole-Based Porous Carbons for
510 CO₂ Capture. *Adv Funct Mater* 21:2781–2787. <https://doi.org/10.1002/adfm.201100291>

511 Shen K, Zhang L, Chen X, et al (2018) Ordered macro-microporous metal-organic framework
512 single crystals. *Science* (80-) 359:206–210. <https://doi.org/10.1126/science.aao3403>

513 Sherwood PMA (1976) X-ray photoelectron spectroscopic studies of some iodine compounds. *J*

514 Chem Soc Faraday Trans 2 72:1805. <https://doi.org/10.1039/f29767201805>

515 Song J-R, Duan W-G, Li D-P (2018) Synthesis of Nitrogen-Rich Polymers by Click
516 Polymerization Reaction and Gas Sorption Property. *Molecules* 23:1732.
517 <https://doi.org/10.3390/molecules23071732>

518 Subrahmanyam KS, Malliakas CD, Sarma D, et al (2015) Ion-Exchangeable Molybdenum
519 Sulfide Porous Chalcogel: Gas Adsorption and Capture of Iodine and Mercury. *J Am Chem*
520 *Soc* 137:13943–13948. <https://doi.org/10.1021/jacs.5b09110>

521 Sun F, Yin Z, Wang Q-Q, et al (2013) Tandem Postsynthetic Modification of a Metal-Organic
522 Framework by Thermal Elimination and Subsequent Bromination: Effects on Absorption
523 Properties and Photoluminescence. *Angew Chemie Int Ed* 52:4538–4543.
524 <https://doi.org/10.1002/anie.201300821>

525 Sun H, La P, Yang R, et al (2017) Innovative nanoporous carbons with ultrahigh uptakes for
526 capture and reversible storage of CO₂ and volatile iodine. *J Hazard Mater* 321:210–217.
527 <https://doi.org/10.1016/j.jhazmat.2016.09.015>

528 Wang C, Zheng T, Luo R, et al (2018) In Situ Growth of ZIF-8 on PAN Fibrous Filters for
529 Highly Efficient U(VI) Removal. *ACS Appl Mater Interfaces* 10:24164–24171.
530 <https://doi.org/10.1021/acsami.8b07826>

531 Xiao Z, Xiao G, Shi M, Zhu Y (2018) Homogeneously Dispersed Co₉S₈ Anchored on
532 Nitrogen and Sulfur Co-Doped Carbon Derived from Soybean as Bifunctional Oxygen
533 Electrocatalysts and Supercapacitors. *ACS Appl Mater Interfaces* 10:16436–16448.
534 <https://doi.org/10.1021/acsami.8b01592>

535 Yang SJ, Kim T, Im JH, et al (2012) MOF-Derived Hierarchically Porous Carbon with
536 Exceptional Porosity and Hydrogen Storage Capacity. *Chem Mater* 24:464–470.
537 <https://doi.org/10.1021/cm202554j>

538 Yin Z, Wang Q-X, Zeng M-H (2012) Iodine Release and Recovery, Influence of Polyiodide
539 Anions on Electrical Conductivity and Nonlinear Optical Activity in an Interdigitated and
540 Interpenetrated Bipillared-Bilayer Metal–Organic Framework. *J Am Chem Soc* 134:4857–
541 4863. <https://doi.org/10.1021/ja211381e>

542 Yu F, Li D-D, Cheng L, et al (2015) Porous Supramolecular Networks Constructed of One-
543 Dimensional Metal–Organic Chains: Carbon Dioxide and Iodine Capture. *Inorg Chem*
544 54:1655–1660. <https://doi.org/10.1021/ic502650z>

545 Zhou J, Hao S, Gao L, Zhang Y (2014) Study on adsorption performance of coal based activated
546 carbon to radioactive iodine and stable iodine. *Ann Nucl Energy* 72:237–241.
547 <https://doi.org/10.1016/j.anucene.2014.05.028>

548

549

550

551

552

553

554

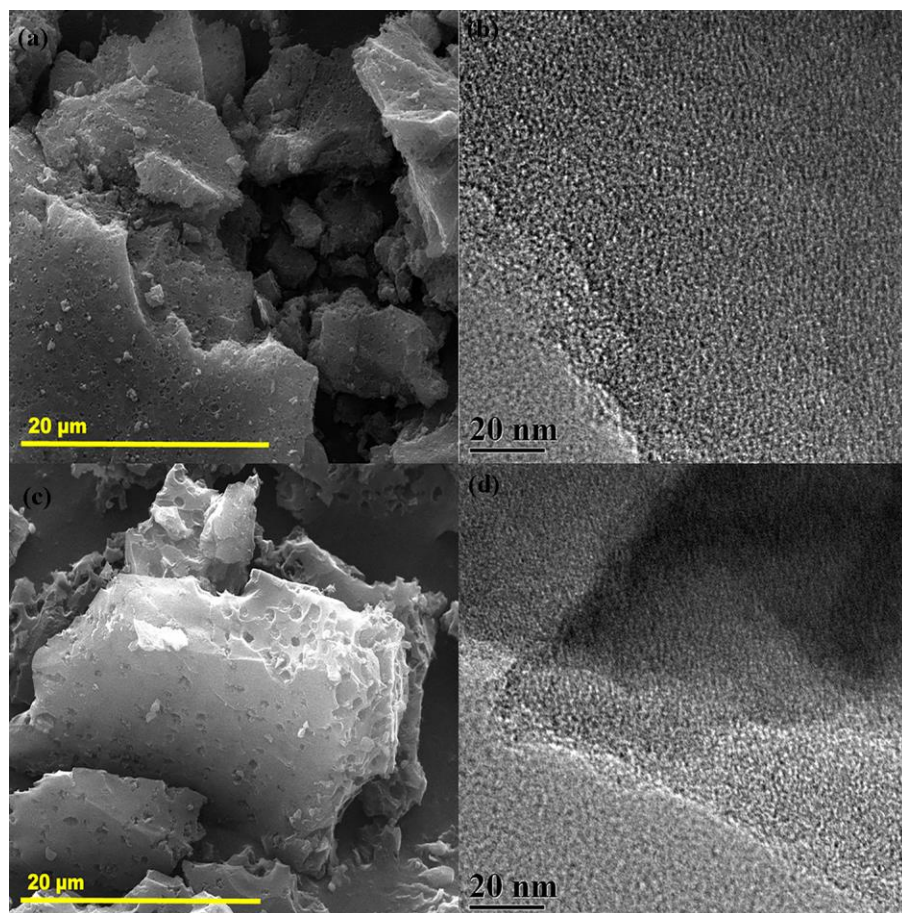
555

556

557

558 **Figures**

559

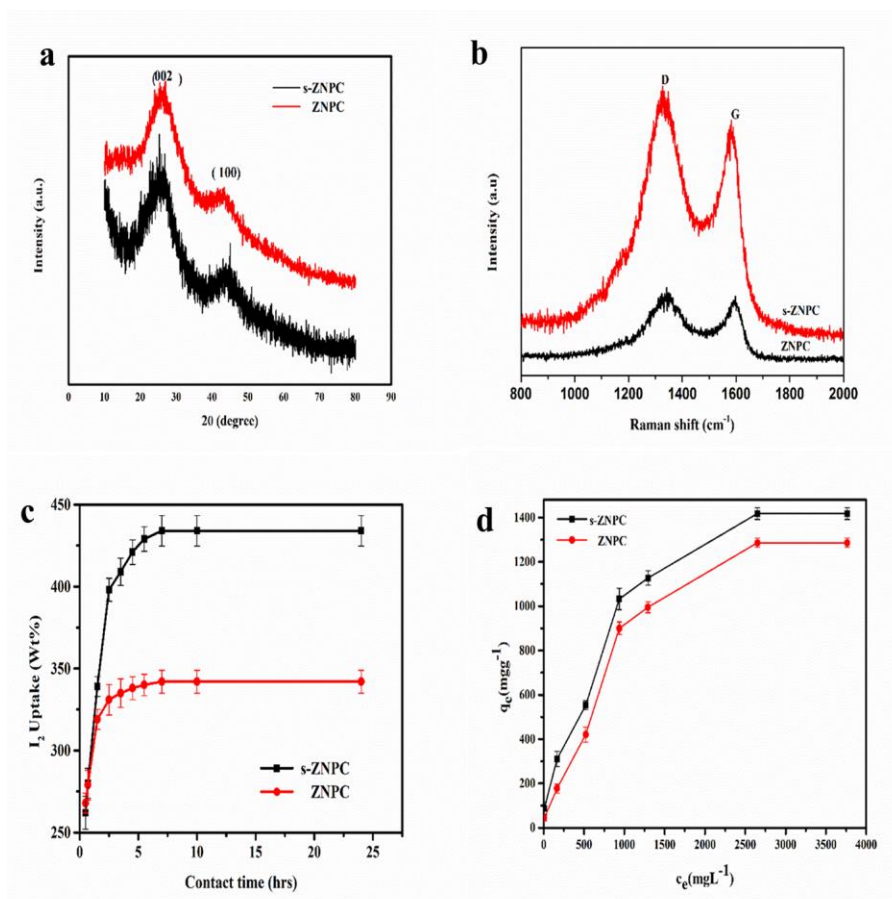


560

561

562 **Fig. 1.** Morphological studies of as-prepared materials showing (a) SEM and (b) TEM of s-
563 ZNPC and (c) SEM and (d) TEM of ZNPC

564

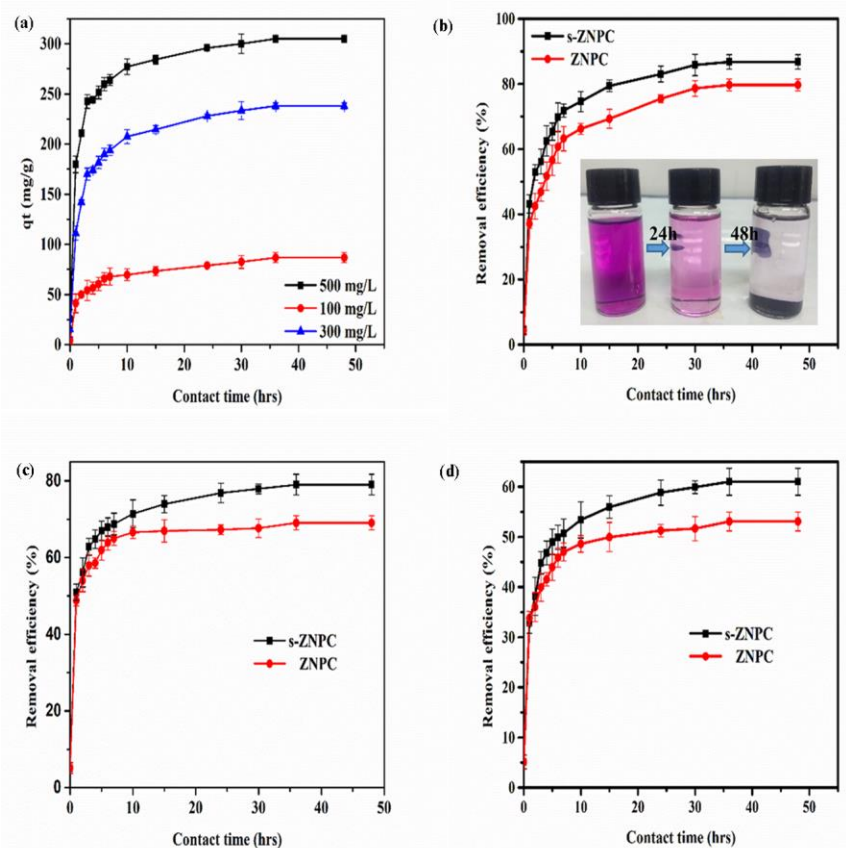


565

566

567 **Fig. 2.** (a) XRD and (b) Raman spectra of s-ZNPC and ZNPC, (c) Gravimetric radioiodine
 568 uptake at 353K by s-ZNPC and ZNPC and (d) adsorption equilibrium isotherm showing
 569 maximum adsorption capacity for radioiodine. Error bars were calculated with the standard
 570 deviation of triplicate measurements at 95% confidence level

571



572

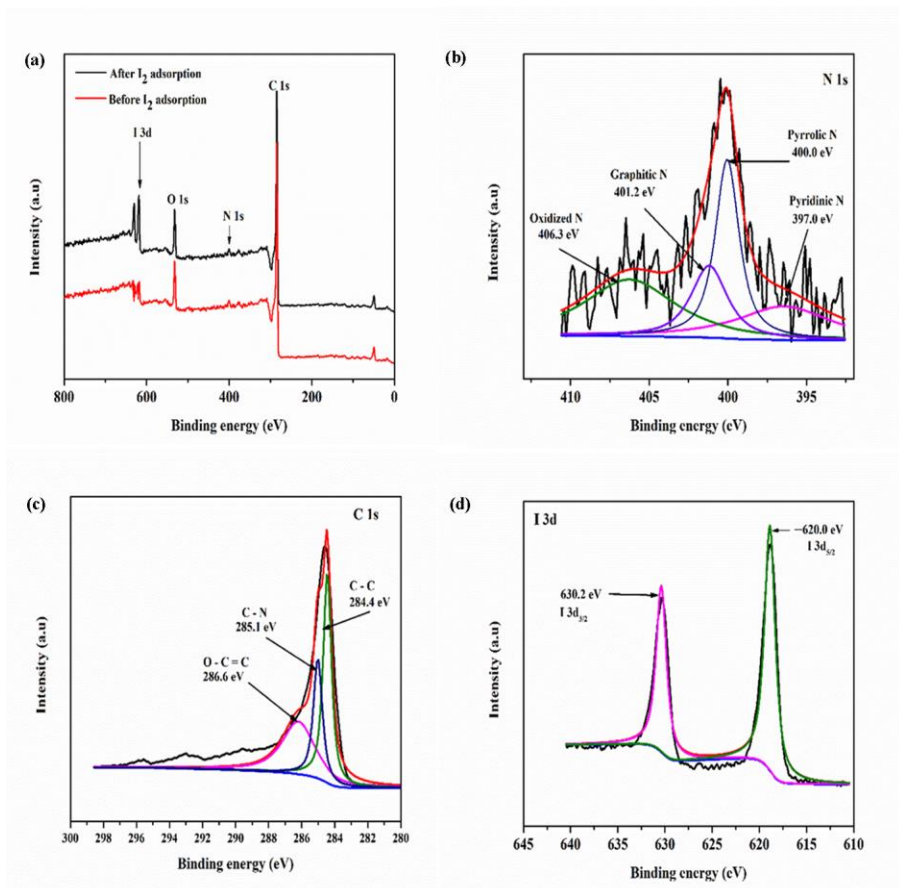
573 **Fig. 3.** Kinetic studies of I₂ adsorption by s-ZNPC and ZNPC: (a) Amount of Iodine removed by
 574 s-ZNPC in 100, 300 and 500 mg/L Iodine/cyclohexane solutions (b) I₂ removal efficiency in 100
 575 mg/L I₂/cyclohexane solution, (inset: color change of solution over time); (c) Radioiodine
 576 removal efficiency in 300mg/L solution; (d) Radioiodine removal efficiency in 500 mg/L
 577 cyclohexane solution. The error bars were calculated with standard deviation of triplicate
 578 measurements at 95% confidence level

579

580

581

582



583

584 **Fig. 4.** XPS studies of s-ZNPC and I₂@s-ZNPC showing (a) survey spectra before (s-ZNPC) and

585 after (I₂@s-ZNPC) iodine adsorption; (b) deconvoluted N 1s spectra; (c) C 1s spectra; (d) I 3d

586 spectra

587

588

Figures

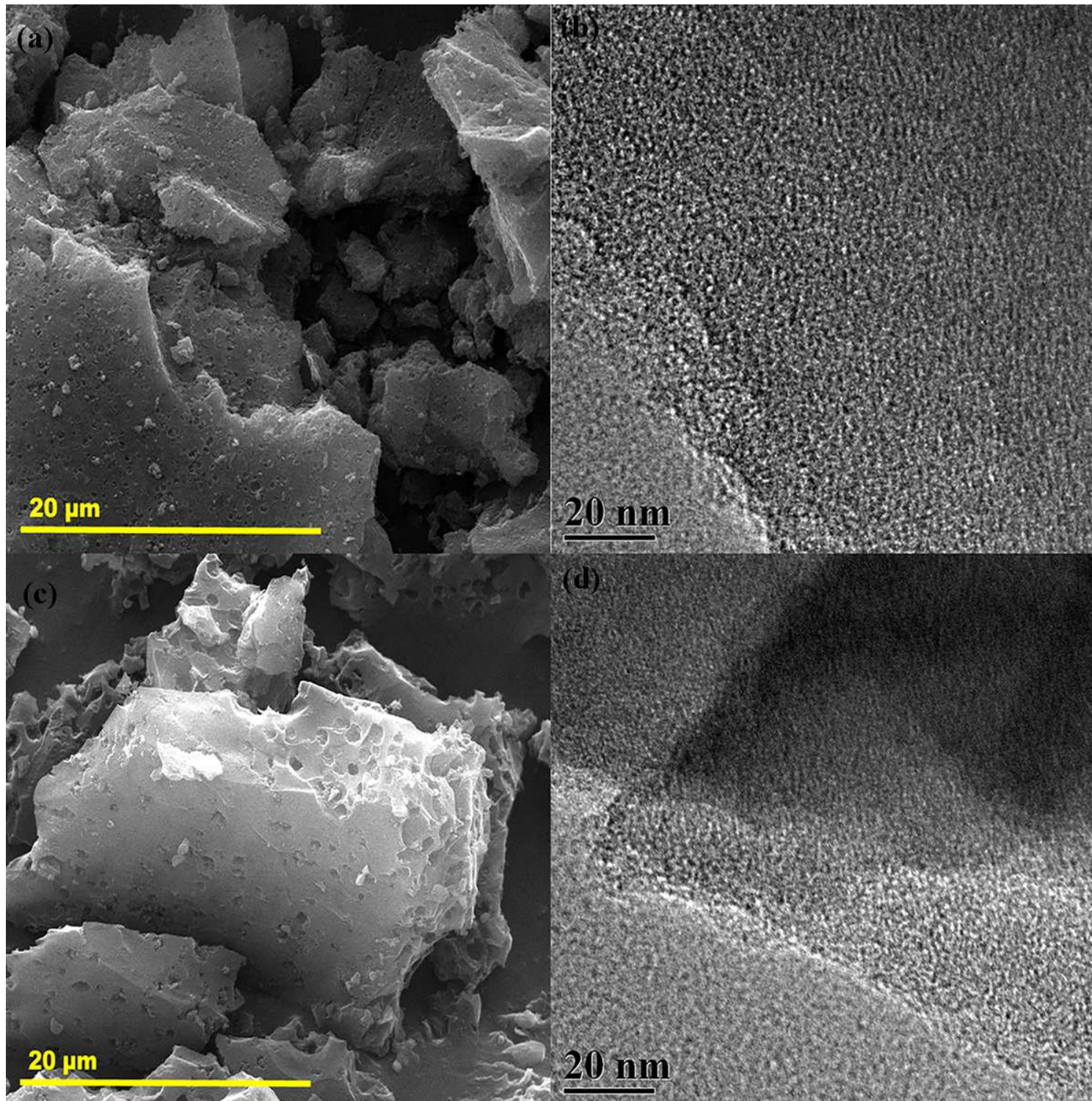


Figure 1

Morphological studies of as-prepared materials showing (a) SEM and (b) TEM of s-ZNPC and (c) SEM and (d) TEM of ZNPC

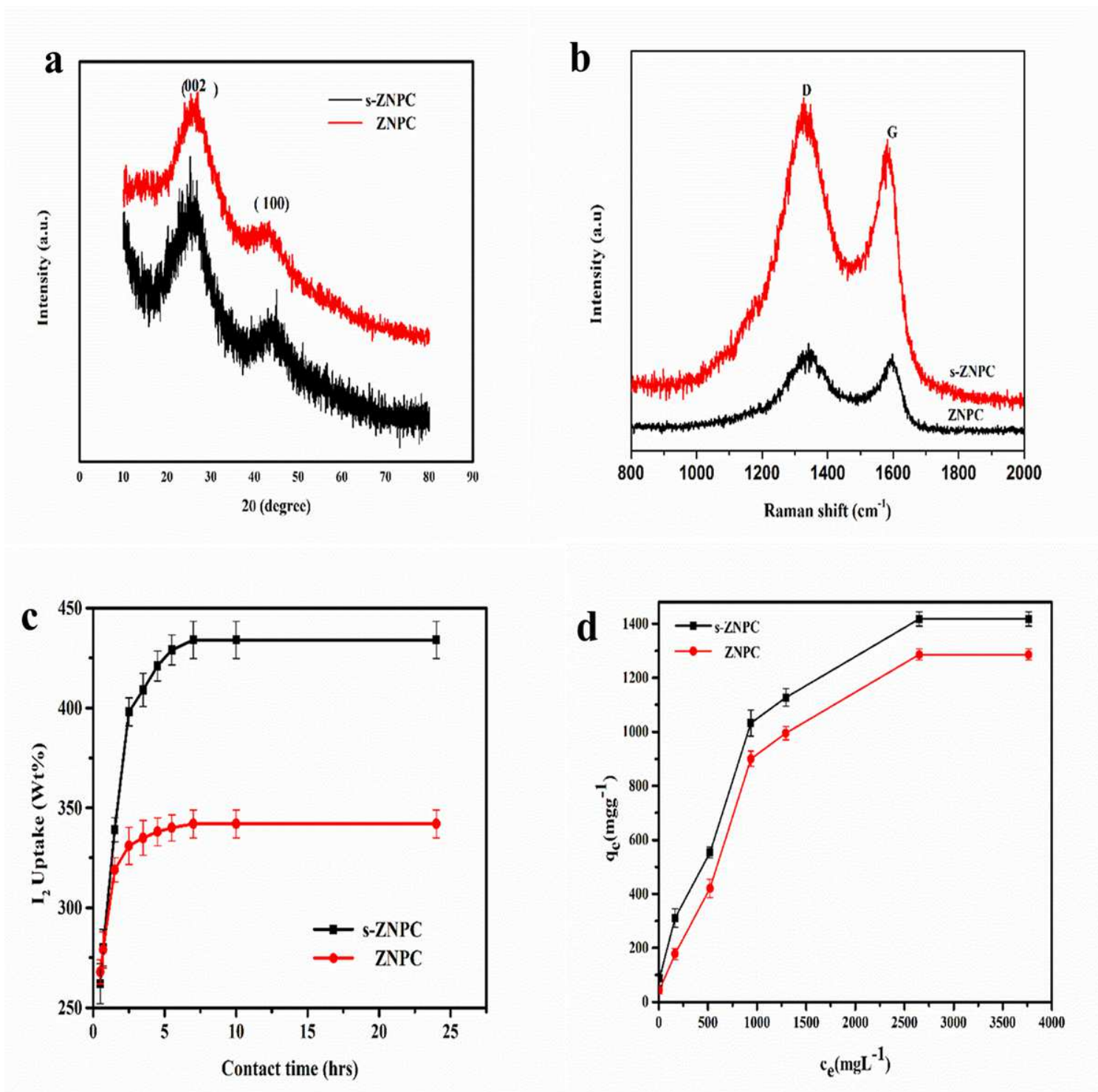


Figure 2

(a) XRD and (b) Raman spectra of s-ZNPC and ZNPC, (c) Gravimetric radioiodine uptake at 353K by s-ZNPC and ZNPC and (d) adsorption equilibrium isotherm showing maximum adsorption capacity for radioiodine. Error bars were calculated with the standard deviation of triplicate measurements at 95% confidence level

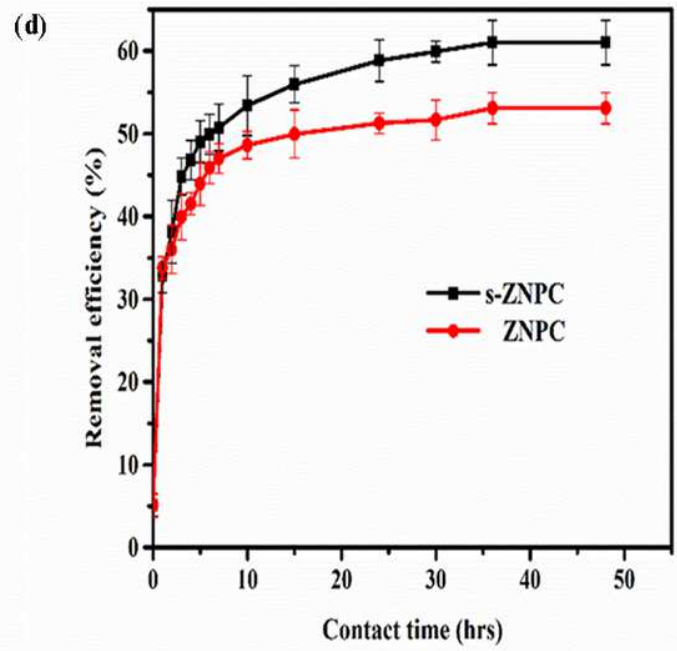
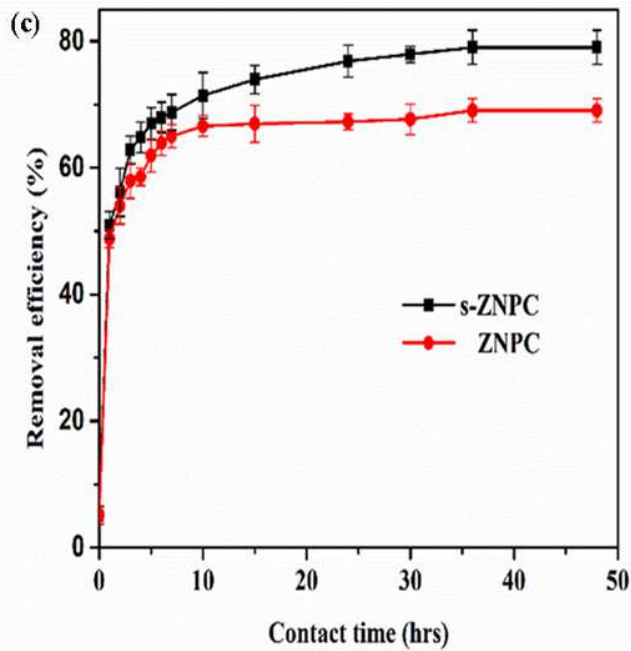
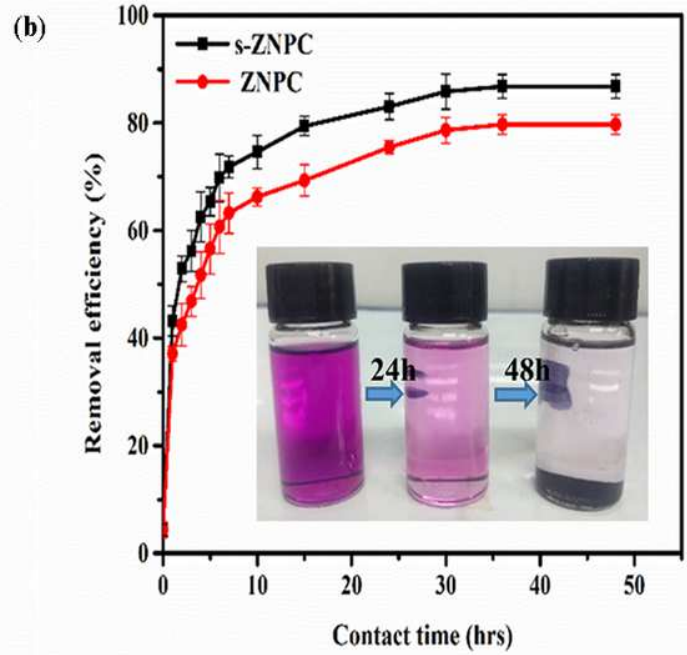
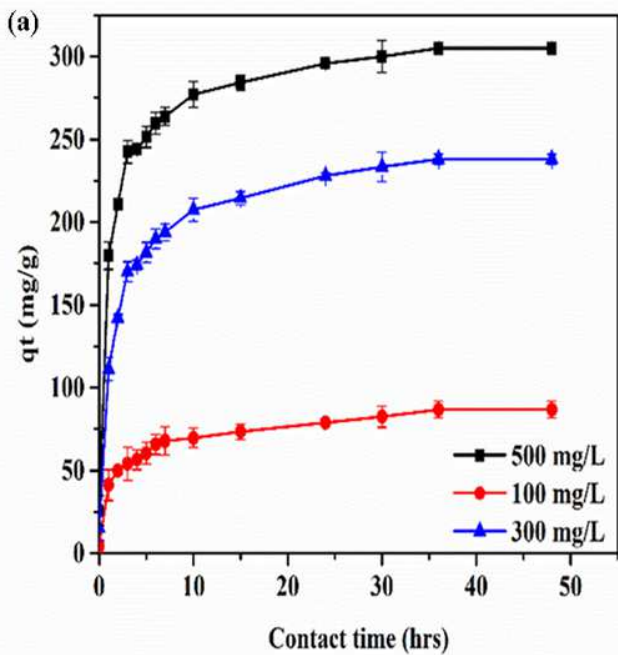


Figure 3

Kinetic studies of I2 adsorption by s-ZNPC and ZNPC: (a) Amount of Iodine removed by s-ZNPC in 100, 300 and 500 mg/L Iodine/cyclohexane solutions (b) I2 removal efficiency in 100 mg/L I2/cyclohexane solution, (inset: color change of solution over time); (c) Radioiodine removal efficiency in 300mg/L solution; (d) Radioiodine removal efficiency in 500 mg/L cyclohexane solution. The error bars were calculated with standard deviation of triplicate measurements at 95% confidence level

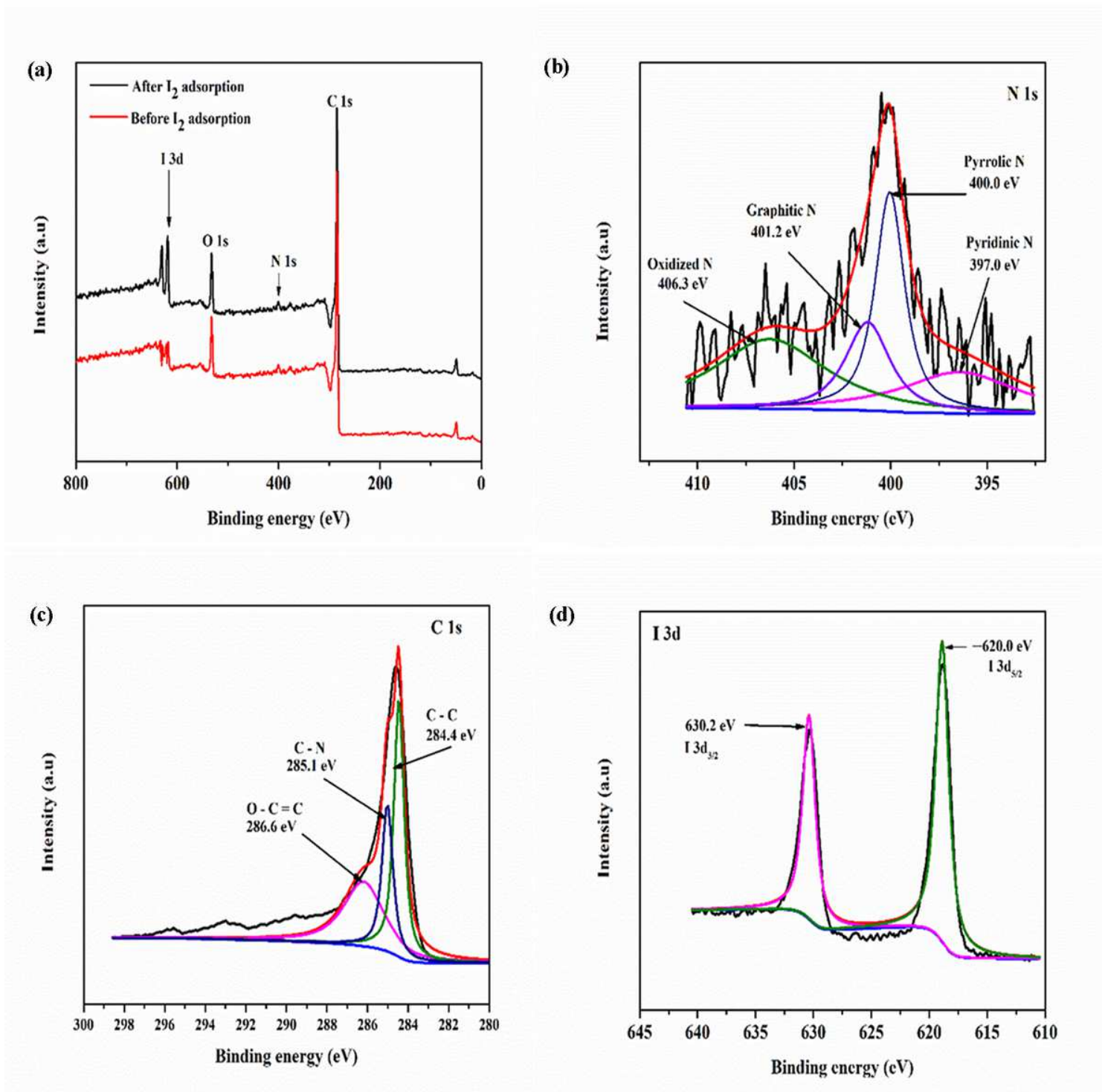


Figure 4

XPS studies of s-ZNPC and I₂@s-ZNPC showing (a) survey spectra before (s-ZNPC) and after (I₂@s-ZNPC) iodine adsorption; (b) deconvoluted N 1s spectra; (c) C 1s spectra; (d) I 3d spectra

Supplementary Files

This is a list of supplementary files associated with this preprint. Click to download.

- [SupplementaryInformation.docx](#)